INTERNATIONAL JOURNAL FOR NUMERICAL METHODS IN FLUIDS, VOL. 12, 655–682 (1991)

A TWO-PHASE, TWO-COMPONENT MODEL FOR NATURAL CONVECTION IN A POROUS MEDIUM

P. A. FORSYTH AND R. B. SIMPSON

Department of Computer Science, University of Waterloo, Waterloo, Ontario, Canada N2L 3G1

SUMMARY

A numerical study of natural convection in a two-phase, two-component flow in a porous medium heated from below is presented. Interphase mass and energy transfer, latent heat and bouyancy effects are major physical features. This study extends earlier studies of natural convection based on single-phase, saturated porous medium models. The appearance of two-phase heat pipe zones in the flow has a marked effect on the fluid and heat flows as well as on the performance of the numerical methods. The numerical techniques for handling phase change, Jacobian construction and time step selection are discussed.

KEY WORDS Two-phase Porous medium Convection Heat pipe

1. INTRODUCTION

The heat transfer across a layer of fluid in a porous medium which is heated from below has been extensively studied using a model based on a single liquid phase saturating the porous medium. From a heat transfer point of view, this model exhibits two basic regimes: the conductive regime at low bottom heating, in which the heat is transferred primarily by conduction and the liquid's motion is absent or secondary; and the convective regime for higher bottom heating, in which the liquid flows in convection cells or irregular quasi-periodic flows which are the primary mechanisms of heat transfer across the layer. The literature of this model is reviewed in Section 1.1 below.

The validity of the single-phase model becomes increasingly questionable with increasing bottom heating, since for real fluids the higher temperatures may exceed the saturation temperature of the liquid phase unless the layer is subjected to increasing pressure. In this paper we extend these studies by employing a more complex model for the fluid which consists of two chemical components, water and air, and two physical phases, liquid and vapour. The model simulates the flow of fluid and energy through both the water-saturated zone and the overlying unsaturated zone of a rock matrix uniformly heated from below. With the bottom temperature of the layer as the basic parameter of the study, the flow is studied dynamically, starting from a standard conductive state (properties varying with depth only). Although the extended model poses a significantly larger computation than its single-phase predecessor, the increased computing power provided by current developments in computational techniques (as discussed in Section 2) and in processors makes this model viable even for relatively inexpensive and commonly available workstations.

For the range of bottom heating used in our study, this model exhibits three heat transfer regimes, which have been identified by Hardee and Nilson.[1] The first two of these, in order of increasing bottom heating, are the conductive and liquid phase convective regimes, in which the

0271–2091/91/070655–28$14.00

Received 21 November 1989
Revised 25 May 1990

saturated zone has the characteristics of the single-phase model discussed in the opening paragraph, modified in minor ways by the presence of the air. At higher bottom temperatures, however, the temperature locally in the flow field can rise to, and be limited by, the water saturation temperature at which the water component is partially evaporated and exists in a two-phase state. Such two-phase zones form locally in the liquid phase convection cells of the saturated zone and limit their role in heat transfer while introducing a new heat transfer mechanism, namely a cycle of evaporation, vapour convection and condensation. This regime is referred to as the two-phase convection regime. The role of phase change in the heat and mass transfer by a volatile fluid has been studied under the name of the heat pipe effect. A prominent feature of heat pipes is a counter-current flow between the two phases of one chemical component, i.e. water. The vapour phase rises due to buoyancy, while the liquid phase sinks past it due to gravity. Previous work on heat pipe effects appears to have concentrated on experimental and analytical studies of one-dimensional two-phase zones to predict transport rates and the lengths of the two-phase zones (see Section 1.2 below.) A major feature of this study is the demonstration of the formation of localized two-phase 'pockets' in the convection cells of the saturated zone, with general-two dimensional shapes. These pockets are two-dimensional heat pipes, and modelling a flow in which they develop requires a computational technique which can be applied uniformly and efficiently to both saturated and unsaturated zones.

Section 2 of the paper is devoted to the mathematical model and the numerical solution strategies we have used to meet these challenges. The geometry and equations for the two-phase, two-component model are described first. The layer is confined to a box 60 m deep by 90 m wide and the rock matrix void is filled two-thirds with water and one-third with air. The top of the box is held at 20 °C and the evolution of the dynamic model to a steady state for bottom temperatures in the range 70–150 °C has been computed.

The equations involve eight state variables, with three evolutionary partial differential equations and five algebraic equations. The flow bed is discretized into square cells and the equations are discretized in time by a fully implicit method and in space by a conservative finite volume scheme, as discussed further in Section 2.1. The resulting algebraic equations are solved in Section 2.2 by the full Newton method using a preconditioned conjugate residual iteration to solve the linear systems of equations. Numerical differentiation is used to produce an effective approximation to the Jacobian matrix for Newton's method. In Section 2.3 we discuss how the structure of the discretized conservation laws allows us to compute the Jacobian matrix very economically. This procedure also substantially simplifies the incorporation or modification of complex physical relationships for transport coefficients or the thermodynamics in the model. As a result, there is little reason for us to use simplifying assumptions such as the Boussinesq approximation in our computation.

The primary variables are the three state variables that are advanced in time by solving the discretized conservation laws. While two of these are always the pressure and the temperature, the goal of having a uniform computational technique for the entire fluid is complicated by the fact that the third primary variable, for a given cell, depends on the liquid saturation condition of this cell. Accommodating phase changes at arbitrary locations in the flow field complicates the numerical procedure, basically because the non-linear model equations do not have a reliable linearization in the presence of extensive phase changes. Emphasis should be placed on 'changes' here, since it is not the presence of two phases in the flow that makes linearization difficult but the possibility of phase change at physically realizable nearby flows that reduces the reliability of linearizations as needed for Newton's method. These computational difficulties underlie the discussions of primary variable selection and switching in Section 2.4 and the time step selection strategy presented in Section 2.5, as well as the discussion of Section 4.1.

Useful summaries of the dynamical state of the flow are provided by the rates of heat transfer into the layer through the bottom, $Q_{bot}(t)$, and out through the top, $Q_{top}(t)$. These symbols are defined more precisely in Section 3. When the bottom heating is low enough that the layer remains in the conductive regime, $Q_{bot}(t)$ and $Q_{top}(t)$ approach each other monotonically. The development of convection cells in the liquid phase can be viewed as a dynamic instability of the conduction regime at higher bottom heating. The onset of this instability is clearly marked in the profile of $Q_{bot}(t)$ by the start of a pulse, shown in Figure 4 of Section 3, as the layer takes in energy to drive the convection cell formation. The pulse in $Q_{bot}(t)$ peaks and then decays to the steady state where it coincides with $Q_{top}(t)$. The physical mechanism of this pulse is explained in Section 3.1. By contrast, the transition from the liquid phase convection regime to the two-phase convection regime is not reflected in these profiles. This is discussed in Section 3.2 and is apparently of a different character than the instability that marks the transition from conductive to convective regimes.

Some concluding observations are made in Section 4; the problems of controlling the time step and our approach to it are discussed in Section 4.1, and in Section 4.2 the heat transfer characteristics of the extended model are described.

1.1. Single-phase studies

The heat transfer across a layer, heated from below, of a single liquid phase saturating a porous medium has been extensively studied and reported in the literature. The models employed usually incorporate the conservation of mass and of energy, Darcy's law for fluid flux and the Boussinesq approximation for buoyancy. The model equations are the evolutionary partial differential equations for the streamfunction and for the temperature, and the flow is studied in an impermeable box with insulated side walls and isothermal top and bottom walls relative to gravity.

After non-dimensionalizing, the temperature differential across the layer appears in the Rayleigh number parameter Ra of the temperature equation. Earlier studies of two-dimensional flows in sealed boxes of rectangular cross-section have been referenced and reviewed by Caltagirone,[2] in the survey article by Combarnous and Bories[3] and, with applications to geothermal systems, by Cheng.[4]

The basic phenomenon of this literature for a horizontal layer is that as Ra increases past a critical Rayleigh number Ra(crit), solutions of the model equations corresponding to two-dimensional convection cells, or rolls, bifurcate from the simple conduction solution. The convection cells transfer heat across the layer more efficiently than conduction alone, and the ratio of the heat transferred via the convection solution to that transferred via conduction only is the Nusselt number. The above-referenced literature studies the critical Rayleigh number, the influence of box geometry on it, the stability of the convection cells and the corresponding heat transfer, summarized by graphs showing Nusselt number as a function of Rayleigh number.

The 'sealed box' model assumption of an impermeable top and bottom for the box containing the flow is central to the value, and even existence, of a critical Rayleigh number Ra(crit), above which the conduction solution loses stability and convection cells form. The influence of the boundary conditions on Ra(crit) for this simple model has been discussed in an early paper by Nield.[5] Using a linearized stability analysis of the conduction state (i.e. isothermal top and bottom), Nield reproduced the earlier result that for fixed temperature boundaries at the top and bottom which are rigid to fluid motion, $Ra(\text{crit}) = 4\pi^2$. He further showed that if the top layer is relaxed to allow a specified heat flux, Ra(crit) is reduced to 27·1, and if it is further relaxed to also allow a constant-pressure upper surface, Ra(crit) is reduced to 9·87 (i.e. π^2).

More recently, the stability of the convection cells under the perturbing effect of tilting the layer relative to gravity has been studied by Moya *et al.*,[6] Sen *et al.*[7] and Caltagirone and Bories.[8] This last reference analyses three-dimensional convection cells as well as two-dimensional rolls.

The loss of stability of these cells through Hopf bifurcation to quasi-periodic solutions as *Ra* increases has also been studied by Caltagirone,[2] by Borkowska-Pawlak and Kordylewski[9] and, more recently, in terms of the 'cascading' of bifurcations for very large Rayleigh numbers by Kimura *et al.*[10]

Rao *et al.*[11] extended this line of study to a more complex geometry by studying cellular flows in a horizontal annulus. In a study directed towards modelling geophysical gas dynamics, Davidson[12] computed the stability of formation of a single convection cell in the vapour phase of a porous flow overlying a liquid pool with an isothermal surface.

These references have in common that they are studies of the formation of cellular convective flows in a single saturating phase under buoyant heating and that they employ the streamfunction–temperature pair of partial differential equations as the basic mathematical model. This pair of equations reflect linear, constant-coefficient material properties except for the non-linearity associated with the buoyant convection-coupling terms.

More physical features are present in the multicomponent, single-phase model of Lai *et al.*[13] based on three transport equations for three model variables, i.e. pressure, temperature and concentration of a chemical species. The saturated zone flow dynamics is computed by the coupled pressure and temperature equations, and the transport of the passive chemical component is included. Operator splitting of diffusive and convective transport is used, which allows careful consideration of errors due to discretization of the convective transport terms. It also permits the implicit equation solving to be limited to the diffusive transport terms, which are basically linear. Among the numerical tests reported in this paper is a study of a thermal cell in a porous slab driven by side wall heating, for Rayleigh numbers in the range 25–200, which exhibits strong convection at the upper end of this range.

1.2. Multiphase review

Two departures from the relatively simple equations used for the models for the studies of Section 1.1 will be reviewed in this subsection: the inclusion of phase change for the fluid, which introduces additional variables and algebraic thermodynamic equations and constraints; and the inclusion of unsaturated flows, which introduces non-linear permeabilities as well as additional variables and equations.

Two papers from 1977, by Sondergeld and Turcotte[14] and Hardee and Nilson,[1] provide qualitative and experimental insights into some implications of phase change for the flow. In the first of these the authors report on experiments in which a water-saturated layer in a bed of sand was heated from below to form a two-phase zone. Their study reports the formation of convection cells in a saturated liquid zone, like those referred to in the above review of single-phase flows, above a hot two-phase zone. The paper observes that: 'The two phase region was of variable geometry and had a distinctly non-horizontal steam–water interface with the overlying water zone. Convective instabilities were initiated by the occurrence of the phase change'. The paper concludes with a discussion of applications to explaining geological formations. The question of the stability of a two-phase zone below a liquid-saturated zone which is raised by Sondergeld and Turcotte is also addressed by Schubert and Straus.[15] The authors discuss configurations of geothermal fields, present a linearized stability analysis of two horizontal layers, the lower being a two-phase zone, and conclude that such layers can be stable for sufficiently small permeabilities.

In a study motivated by modelling nuclear reactor accidents, Hardee and Nilson[1] qualitatively identify three heat transfer regimes closely connected with those discussed in this paper, and

derive algebraic relations for the heat transfer parameters based on macroscopic heat and mass balance arguments for a single convection cell with internal heating of the fluid. Although a major contribution of the paper is its reporting of experimental results, these are not closely related to this study since they are carried out in a cylindrical apparatus, with heat generation distributed in the flow field, and in a high-permeability medium.

Experimental measurements of the characteristics of heat pipes and one-dimensional models for them are reported by Bau and Torrance[16] and Udell[17] based on a cylindrical apparatus. The former paper reports long-term fluctuations in the temperature profile in the two-phase zone underlying a liquid-saturated layer, suggesting that the two-phase zone may not have a stable steady state but may have a stable periodic or quasi-periodic state. The authors also point out that the overlying saturated layer can be viewed as a single-phase layer heated from below, as discussed in the previous subsection. However, permeable, constant-pressure boundary conditions are more appropriate than 'sealed box' impermeable boundaries for this context, and as mentioned in Section 1.1,[5] such a layer is unstable, i.e. develops convective solutions, for any temperature differential across it.

The mathematical analyses of these heat pipe flows have been carried out using one-dimensional models for the counter-current flows of the two phases of a single saturating component (water), and analytical derivations of model properties.

Two-dimensional mathematical models which are similar to those presented in Section 2 below have been used to study the evolution of the unsaturated porous flow field about a nuclear waste repository by Pollock[18] and Tsang and Pruess.[19] Two-phase, multicomponent models are used in the simulation of geothermic fields, where typically the dynamic effect of a well bore on a flow field is studied; see the survey article by Pruess[20] and its bibliography.

We can identify and distinguish the role of this study in relation to those reviewed above by noting that we are studying the stability and heat transfer phenomena of the formation of convection cells under buoyant heating, which is the subject of the single-phase studies reviewed in Section 1.1. However, instead of the streamfunction–temperature pair of equations appropriate to the single-phase models used in those studies, we are using the extended equations for multiphase, multicomponent flows. That is, the primitive variable transport equations are solved in conjunction with the algebraic relations and constraints governing two chemical components and the thermodynamics of phase change, which allows a uniform treatment of saturated and unsaturated zones. These equations admit the phenomena of the modelling described in this subsection, in particular the formation of heat pipes. They do, however, pose numerical solution difficulties beyond those of the simpler equations of Section 1.1 and which are discussed in detail in the sequel.

2. THE MATHEMATICAL MODEL

The following glossary of symbols will be used to describe the mathematical model:

S_m	saturation of phase $m=1$, g (liquid, gas)
P	pressure (kPa)
T	temperature (K)
K	absolute permeability (m^2)
K_{rm}	relative permeability of phase m
μ_m	viscosity of phase m (kPa day)
U_m	internal energy of phase m (J $mole^{-1}$) (R = rock)
h_m	enthalpy of phase m (J $mole^{-1}$)
M_m	molar density of phase m (mole m^{-3})

ϕ porosity
λ_H composite heat conductivity (J m^{-1} day^{-1} K^{-1})
D_g gas phase diffusivity (m^2 day^{-1})
ρ_m mass density of phase m (kg m^{-3})
g acceleration due to gravity (m s^{-2})
d depth (m)
Y_p mole fraction of component p in the gas phase
X_p mole fraction of component p in the liquid phase.

These symbols can be divided into variables for which the evolution is to be computed by the model, and parameters, including possibly non-linear functions, which are to be specified for the model. The variables are S_g, S_l, X_a, X_w, Y_a, Y_w, P and T, and the parameters and their specifications are given in Appendix I.

For the description of the conservation laws of the model, it is convenient to combine the mechanical driving forces of pressure and buoyancy for the liquid and gas phases into phase potentials. The gradients of these potentials are defined by

$$\nabla\psi_l = \nabla P - \rho_l g \nabla d, \qquad \nabla\psi_g = \nabla P - \rho_g g \nabla d. \tag{1}$$

We have assumed here that the capillary pressure $P_l - P_g$ is small and consequently $P_l = P_g = P$ is a satisfactory modelling approximation. Following Forsyth[21] and using the phase potentials of (1), the basic conservation equations, based on the multiphase form of Darcy's law, can be written as follows:

conservation of air

$$\frac{\partial}{\partial t}[\phi(S_l M_l X_a + S_g M_g Y_a)] = \nabla\cdot\left(M_l X_a \frac{KK_{rl}}{\mu_l}\nabla\psi_l\right) + \nabla\cdot\left(M_g Y_a \frac{KK_{rg}}{\mu_g}\nabla\psi_g\right) + \nabla\cdot(D_g M_g \nabla Y_a); \tag{2}$$

conservation of water

$$\frac{\partial}{\partial t}[\phi(S_l M_l X_w + S_g M_g Y_w)] = \nabla\cdot\left(M_l X_w \frac{KK_{rl}}{\mu_l}\nabla\psi_l\right) + \nabla\cdot\left(M_g Y_w \frac{KK_{rg}}{\mu_g}\nabla\psi_g\right) + \nabla\cdot(D_g M_g \nabla Y_w); \tag{3}$$

conservation of energy

$$\begin{aligned}\frac{\partial}{\partial t}[\phi(S_l M_l U_l + S_g M_g U_g) + (1-\phi)U_r M_r] = {} & \nabla\cdot\left(h_l M_l \frac{KK_{rl}}{\mu_l}\nabla\psi_l\right) \\ & + \nabla\cdot\left(h_g M_g \frac{KK_{rg}}{\mu_g}\nabla\psi_g\right) + \nabla\cdot(D_g M_g h_{gw}\nabla Y_w) \\ & + \nabla\cdot(D_g M_g h_{ga}\nabla Y_a) + \nabla\cdot(\lambda_H \nabla T).\end{aligned} \tag{4}$$

In addition to these conservation laws, the equilibrium thermodynamics determines the following two relations:

$$Y_a = Z_a(P, T)X_a, \qquad Y_w = Z_w(P, T)X_w. \tag{5}$$

The functional dependence of Z_a and Z_w on P and T is given in Appendix I.

For each of the three physically meaningful phase states that the model fluid can take on, the model variables must satisfy the corresponding equations and inequalities:

the liquid-saturated state

$$S_l = 1, \qquad S_g = 0, \qquad X_a + X_w = 1, \qquad Y_a + Y_w \leqslant 1; \tag{6a}$$

the vapour–liquid mixed state

$$S_g + S_l = 1, \quad X_a + X_w = 1, \qquad Y_a + Y_w = 1, \qquad S_l > 0, \qquad S_g > 0; \tag{6b}$$

the gas-saturated state

$$S_l = 0, \qquad S_g = 1, \qquad Y_a + Y_w = 1, \qquad X_a + X_w \leqslant 1. \tag{6c}$$

It will be seen that (2)–(5) plus the appropriate version of (6) form a system of eight algebraic and partial differential equations for the eight evolutionary variables. Further details of the selection of variables for computing their evolution are given in Section 2.4.

The model is posed for a rock matrix bed 90 m wide (chosen as the x-direction) by 60 m deep (chosen as the z-direction) with all properties and variables assumed to be constant in the horizontal y-direction. The initial configuration is illustrated in Figure 1, showing that the bottom approximately two-thirds are saturated with water ($S_l = 1{\cdot}0$) and the top third is at the residual unsaturated value ($S_l = 0{\cdot}1$) The boundary conditions are chosen so that the saturated zone resembles closely the fluid of the single-phase saturated zone studies reviewed in Section 1.1, i.e. the domain of the flow is an impermeable box with insulated sides. The temperature at the top of the layer is maintained at a constant T_{top}, taken to be 20 °C in this study, and the temperature at the bottom of the layer is a parameter of the study and is varied between 70 and 150 °C. For a steady state bottom temperature T_{bot} in excess of 142 °C, a dynamic bottom temperature was used which decayed exponentially from 142 °C to T_{bot} with a time constant of 35 days, i.e.

$$T_{bot}(t) = \begin{cases} T_{bot} & \text{if } T_{bot} \leqslant 142\,^{\circ}\text{C}, \\ T_{bot}[1 - w(t)] + 142 w(t) & \text{if } T_{bot} > 142\,^{\circ}\text{C}, \end{cases}$$

where

$$w(t) = \exp(-t/35),$$

with t measured in days.

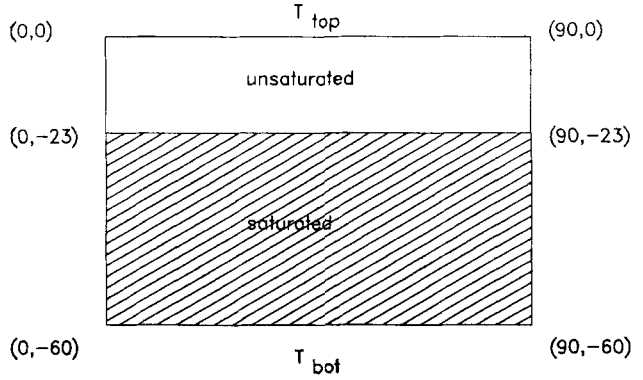

Figure 1. Extended model geometry

The choices of the cut-off temperature at 142 °C and the time constant of 35 days in this dynamic boundary condition are pragmatic choices without particular physical significance. Basically, using the time step selection procedure described in Section 2.5, the model was able to start without using excessively small time steps for bottom temperatures up to about 142 °C, but beyond that the procedure selects increasingly small time steps, down to the size of hours, in its attempt to follow initial transient behaviour that is irrelevant to the desired steady state. The time constant of 35 days is much larger that these unduly small initial time steps, but small enough that the dynamic boundary condition has decayed away well before instability of interest in this study sets in.

The initial pressure field is essentially the hydrostatic one, with $P = 100$ kPa being the 'air' pressure in the unsaturated layer. Because the study uses the sealed box model of the single-phase studies of Section 1.1, the pressure field of the steady state solution is a consequence of the initial conditions and is not determined *a priori*. To reduce the influence of this, we have included a relatively large portion of the overlying unsaturated zone, and as a result the steady state pressure in this zone varies from 100 to 105 kPa over the range of T_{bot} used.

A schematic glimpse of the steady state fluid field for bottom heating in the two-phase convection regime is shown in Figure 2, in advance of the more detailed discussion of Section 3. In this figure, two pockets of mixed phase fluid (primarily liquid water and steam) appear, disrupting the horizontal separation of the vapour and liquid phases shown in Figure 1 that characterizes the flow regimes of lower bottom heating.

2.1. Discretization of the model equations

Each of the three conservation laws equates the time rate of change of the density of a conserved quantity to the sum of divergences of fluxes of that quantity driven by gradients in some or all of phase potentials, gas phase mole fractions or temperature. This form is reflected in a corresponding form for the discretized equations, which are formed by using standard conservative finite differencing based on square control volumes and totally implicit time discretization. A detailed description of the finite difference equations may be found in Reference 21, but the general form can be explained as follows. We will use superscript N to denote the Nth time level of

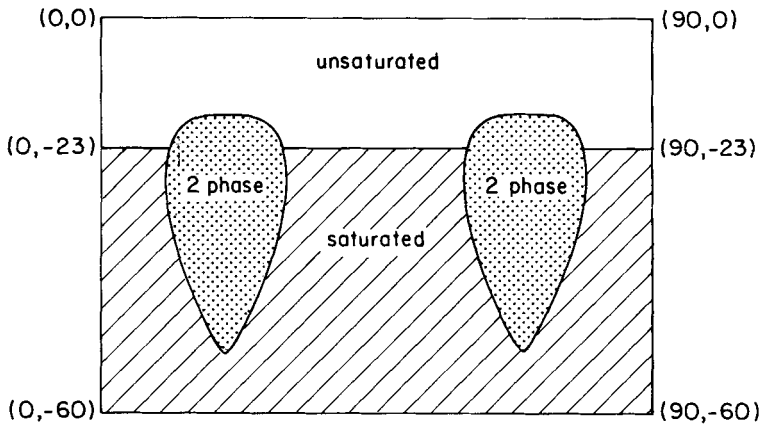

Figure 2. Schematic view of saturation zones for steady state, bottom temperature 150 °C (see Figure 13 for quantitative details)

the discretization and subscript i to denote the ith mesh cell. We will use A_i^N to denote the amount of one of the three conserved quantities considered to be constant in cell i at time N, e.g. for the conservation of water,

$$A_i^N = \phi(S_l M_l X_w + S_g M_g Y_w)_i^N \, \mathrm{Vol}(i),$$

where $\mathrm{Vol}(i)$ is the volume of cell i. The discretized conservation laws then have the form

$$A_i^{N+1} - A_i^N - \Delta t \sum_{j \in \eta_i} [Q_{ji}^{N+1}(A)(\psi_{lj}^{N+1} - \psi_{li}^{N+1}) + R_{ji}^{N+1}(A)(\psi_{gj}^{N+1} - \psi_{gi}^{N+1}) + S_{ji}^{N+1}(A)(Y_{aj}^{N+1} - Y_{ai}^{N+1}) + U_{ji}^{N+1}(A)(Y_{wj}^{N+1} - Y_{wi}^{N+1}) + V_{ji}^{N+1}(A)(T_j^{N+1} - T_i^{N+1})] = 0. \quad (7)$$

In (7), η_i is the set of four indices for the four neighbouring cells to cell i, and the terms in the summation represent the rate at which A flows from cell j into cell i as driven by the quantities differenced between cell j and cell i. We will refer to these summation terms as the discrete fluxes of A, e.g. $Q_{ji}^{N+1}(A)(\psi_{l,j}^{N+1} - \psi_{l,i}^{N+1})$ is the discrete flux of A from cell j to cell i due to the differences in liquid phase potential between these cells. The coefficients Q, R, S, U and V, when present, combine the non-linearities of the transport coefficients involving the state variables in cells i and j with geometric factors from these cells. The designation (A) only indicates that the transport coefficient is associated with the conserved quantity A; it is not intended to indicate a direct functional dependence on A as a variable. The transport coefficients in $Q(A)$ and $R(A)$ are upstream-weighted with the upstream direction determined by the liquid and gas phase potentials respectively. For the other coefficients, harmonic averaging is used. Not all of these coefficients are present in each discrete equation, e.g. for the conservation of water, $S_{ij}^{N+1}(A) = 0$ and $V_{ji}^{N+1}(A) = 0$.

2.2. *Solving the implicit equations*

For the time-stepping process we assume that the eight model variables are known for each cell at the Nth time level and that we have a provisional time step Δt to the next time level. If the time step yields a convergent iteration (see Section 2.5), we can compute the eight variables at the $(N+1)$th time level by advancing three of the variables using the discrete conservation laws and then computing the remaining five variables from the algebraic equations (5) and (6). The five latter variables are referred to as secondary variables and the other three as primary variables; pressure and temperature are always primary variables, but the third depends on the phase state as described in Section 2.4 below. Computing the next provisional time step is also a part of each time step as discussed in Section 2.5.

The running times of these simulations are crucially dependent on the solution strategy used for solving the non-linear equations of the discretized conservation laws. These strategies usually involve selecting a linearization technique (outer iteration) and a method for solving the resulting linear equations. Our strategy has been to use the full Newton method for the outer iteration with the incomplete factorization preconditioning plus the ORTHOMIN acceleration version of the preconditioned conjugate residual iteration for the linear equations.[22,23] The reliability of convergence and enhanced time step size provided by Newton's method plus the efficiency of ORTHOMIN make this combination attractive.

Crucial to our use of the full Newton method is the capability of efficient numerical differentiation for approximating the Jacobian matrix of the non-linear system. For the complex exact expressions and empirical dependences of the non-linear transport coefficients and thermodynamic relationships in this multiphase model, the manual evaluation of the analytic derivatives for the Jacobian matrix is a large and error-prone task. The numerical evaluation of the resulting

analytic expressions is expensive in computing time and gives rise to complicated programming expressions which are disincentives to change or experiment with the physical model. We have found that numerical differentiation produces effective approximations to the Jacobian matrix for Newton's method with code that only evaluates the terms in the equations themselves, not the derivatives. This enables us to use a full physical model with little additional effort.

In our monitoring of the performance of this strategy we found that the time required for constructing the linear equations and the time required to solve them were roughly equal.

2.3. Efficient computation of the numerical Jacobian

The special form of the discrete conservation laws permits an elementary reduction in the amount of computation necessary to form their Jacobian numerically. The basic principle of this reduction can be explained with less technical and notational complication if we illustrate the technique for the case of a single primary variable and a single conservation law.

Let u_i stand for the value of the primary variable in cell i and let u denote the M-vector of primary variables for M cells. Let $A_i(u)$ be the amount of the conserved quantity in cell i and let $f_{ji}(u)$, $j \in \eta_i$, be the discrete flux of A from cell j into cell i.

We assume that $A_i(u)$ depends only on u_i; we assume that $f_{ji}(u)$ depends only on u_i and u_j and that this dependence is such that

$$f_{ji}(u) = -f_{ij}(u). \tag{8}$$

These assumptions are met by the finite differences used to construct the discrete form (7) of the conservation laws (2)–(4). Our example conservation law leads us to seek the solution u of a system of M equations of the form

$$g(u) = 0, \tag{9}$$

where

$$g_i(u) = A_i(u) - A_i(u^N) - \Delta t \sum_{j \in \eta_i} f_{ji}(u), \quad i = 1, \ldots, M, \tag{10}$$

and u^N is the M-vector of known primary variable values at the current time t_N. To solve (9) by Newton's method we require the Jacobian matrix J for g, i.e.

$$J_{ik}(u) = \partial g_i(u)/\partial u_k, \quad 1 \leqslant i \leqslant M, \quad 1 \leqslant k \leqslant M. \tag{11}$$

For Newton's method the $(n+1)$th iterate, $u^{(n+1)}$ is computed from the current iterate $u^{(n)}$ by solving the correction equation

$$J(u^{(n)})c = -g(u^{(n)}) \tag{12}$$

and setting

$$u^{(n+1)} = u^{(n)} + c. \tag{13}$$

To numerically approximate the entries of J we use the differencing interval β in the kth coordinate direction e_k, i.e. β is a scalar and e_k is the unit M-vector with all components zero except the kth. Thus

$$e_{ki} = 0, \quad 1 \leqslant i \leqslant M, \quad i \neq k; \qquad e_{kk} = 1. \tag{14}$$

Then

$$\partial g_i(u)/\partial u_k \approx \delta_k(\beta) A_i(u) - \Delta t \sum_{j \in \eta_i} \delta_k(\beta) f_{ji}(u) \tag{15}$$

for

$$\delta_k(\beta)A_i(u)=[A_i(u+\beta e_k)-A_i(u)]/\beta,$$
$$\delta_k(\beta)f_{ji}(u)=[f_{ji}(u+\beta e_k)-f_{ji}(u)]/\beta.$$

The entries in the kth column of J are $\partial g_i(u)/\partial u_k$ for $i=1,\ldots,M$ and we use the approximate values on the right side of (15) for them.

Now,

$$\delta_k A_i(u)=0 \quad \text{unless} \quad i=k \tag{16}$$

and

$$\delta_k f_{ji}(u)=0 \quad \text{unless} \quad i=k \quad \text{or} \quad j=k \quad \text{and} \quad j\in\eta_i. \tag{17}$$

If $i=k$, then the diagonal entry of J is

$$\frac{\partial g_k}{\partial u_k}(u)\approx\delta_k(\beta)A_k(u_k)-\frac{\Delta t}{\beta}\sum_{j\in\eta_k}[f_{jk}(u+\beta e_k)-f_{jk}(u)]. \tag{18}$$

If $j=k$ and $j\in\eta_i$, then there is an off-diagonal entry in the ith row and kth column of J,

$$\frac{\partial g_i}{\partial u_k}(u)\approx-\frac{\Delta t}{\beta}[f_{ki}(u+\beta e_k)-f_{ki}(u)]=\frac{\Delta t}{\beta}[+f_{ik}(u+\beta e_k)-f_{ik}(u)]. \tag{19}$$

Note, however, that the two discrete flux values in the right-hand approximate expression for $\partial g_i(u)/\partial u_k$ in (19) have already appeared as summands in the summation $j\in\eta_k$ in the approximate expression for $\partial g_k(u)/\partial u_k$ in (18). If the evaluation of $g_k(u+\beta e_k)$, $k=1,\ldots,M$, in (10) is regarded as M function evaluations, then it follows that the entire numerical Jacobian can be constructed in $2M$ function evaluations. (This is independent of the number of dimensions!) Note that even if analytic derivatives are used, M function evaluations are required to calculate the residual for Newton's iteration. In the case of P primary variables and P conservations laws, this technique requires only $(P+1)M$ function evaluations per Newton iteration.

2.4. Changes of phase, changes of primary variables and Newton's method

As indicated in Section 2.2, two of the primary variables for each mesh cell are the pressure P and the temperature T, but the third depends on the phase state of the cell as per (6a–c). For a cell in the liquid-saturated state, X_a is used as the third primary variable, and for a cell in the mixed phase state, S_l is used.[24]

From each Newton iteration a new set of values for the primary variables in each cell is computed. These may, however, not be physically permissible values, since they may violate the inequality constraints required in (6) for that state. It is the role of these constraints to signal changes of phase and corresponding changes of primary variables. Figure 3 shows these transitions for the two states that occur in these computations.* For the switch from the liquid-saturated state to the mixed state, Y_a is reset to $1-Y_w$, and in the reverse switch, S_l is reset to unity.

The effect of a switch of primary variables is to change the system of equations to which Newton's method is being applied. This can happen repeatedly in the iterations for one time step,

* If the cell were in the gas-saturated state ($S_l=0$), then Y_a would be selected as the third primary variable; however, in the computations reported here, this state does not occur.

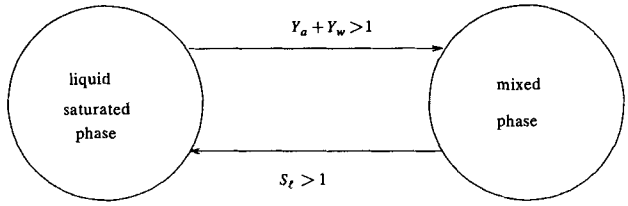

Figure 3. Transition rules for phase change

particularly when the pressure and temperature fields are causing dynamic changes of phase. In this circumstance we do not attain the rapid, quadratic convergence of Newton's method; indeed, the time step must often be reduced to get convergence at all. An obvious alternative switching strategy is to defer the switch until after a time step is completed. However, because a large number of cells may switch in a given time step, this strategy seems to perform poorly compared to allowing switches after every Newton iteration. Deferring the switch until the end of a time step can result in a large number of cells being in thermodynamically inconsistent states, which can result in a highly unstable situation requiring very small time steps. (See, however, Reference 25.)

The change of phase state of a cell from liquid-saturated ($S_l = 1$) to mixed ($0 < S_l < 1$) can happen in several ways. The liquid phase fluxes of the discrete versions of (2)–(4) may result in a net exit of the liquid into neighbouring cells, leaving a previously saturated cell unsaturated. For example, if a saturated cell is above an unsaturated cell with respect to gravity, the liquid will seep from the upper cell to the lower (unless there is some overriding counter-flux). Alternatively, the temperature in a cell may rise to the saturation temperature for the liquid at the pressure in the cell so that some of the liquid is evaporated into the gaseous phase. As indicated in the previous subsection, computationally this can be recognized when the temperature and pressure in a liquid-saturated cell result in $Y_a + Y_w > 1$, which is equivalent to

$$Z_a X_a + Z_w X_w > 1, \tag{20}$$

where Z_a and Z_w are the equilibrium ratios defined in Appendix I.

In the flows of our computations, X_a is very small, so that to a good approximation $X_w = 1$ and the saturation temperature–pressure relation reflected in (20) can be approximated by $Z_w = 1$. Our discussion is complicated by the fact that two conventional but different uses for the term 'saturation' are required: 'saturation' in the porous medium sense and 'saturation' referring to the pressure–temperature condition at which water evaporates. In the hope of reducing possible confusion, we will refer to the temperature above which, at a given pressure, water exists in both vapour and liquid phases as the bubble temperature (for the given pressure) and we will designate it T_{bub}. From $Z_w = 1$, using the formula for Z_w of Appendix I, we conclude that

$$T_{bub} = -30{\cdot}0 + (P \times 10^8/0{\cdot}877)^{1/4{\cdot}76} \quad (^\circ\text{C}). \tag{21}$$

At this temperature, increases in energy in the cell are diverted from raising the temperature of the liquid (increasing its internal energy) to changing its phase, i.e. contributing to the gas phase internal energy in the form of the latent heat of evaporation. Hence the temperature is 'capped' at T_{bub} with regard to further injections of energy, at least until some of the assumptions of (21) are violated. This effect will be seen in the temperature distributions of the two-phase convective flow regime of Section 3.

2.5. *Time step size selection*

The time-stepping procedure can be viewed as attempting to take a time step with a provisional time step, using Newton's method to solve the implicit equations. If Newton's method converges, the provisional time step is accepted and the time variable and solution are updated appropriately. If Newton's iteration fails to converge, the provisional time step is rejected. In either case a new provisional time step is required, which is computed from the previous Newton iteration results, either to repeat the attempt at the current time level or to attempt a step at the newly advanced time level.

The calculation of the new provisional step size is controlled by a fairly complicated set of parameters. For each variable, two parameters are used: the target change parameter, which specifies the desired change in the associated variable per time step; and the convergence tolerance parameter, which is the criterion for convergence of the Newton iteration for the associated variable. A further parameter is the maximum number of iterations allowed, i.e. the Newton iteration is deemed to have converged if the convergence criterion for each variable is met in the specified maximum number of iterations.

If the iteration does not converge, the new provisional step size is a reduction (typically half) of the current rejected step size. If the Newton iteration converges, then for each variable the ratio of the target change parameter to the Newton correction in that variable is computed. The minimum of these ratios is used to multiply the current accepted step size to give the new provisional step size. The intention then is to control the step size so that the Newton corrections hit, or are less than, the target change parameters. An analysis of the error control implications of this kind of strategy is given in Reference 26.

3. FLOW REGIMES

For each value of T_{bot} the flow develops from the common initial state described in the previous section into a dynamic flow/energy transport pattern and ultimately settles into a steady state that is characteristic of T_{bot}. We can identify three basic flow regimes for these flow evolutions:

(i) the conduction regime, in which the dominant heat transfer mechanism is conduction through the liquid phase and rock matrix and the fluid properties vary only with the depth co-ordinate z
(ii) the single-phase convection regime, in which convection cells form in the liquid of the saturated zone and provide significant heat transfer
(iii) the two-phase convection regime, in which two-phase zones of water in the liquid and gaseous phases appear in the saturated layer's convection cells.

Details of these regimes are discussed in the subsections of this section, but we can summarize their relationships as follows. The model is initiated in the conductive regime. If T_{bot} is sufficiently small, the flow remains in this regime throughout its evolution, the fluid properties depending only on the depth co-ordinate z and relaxing monotonically to their equilibrium values. For larger values of T_{bot} the conductive regime is unstable and the flow develops variations in the x-direction which evolve into convection cells. This instability develops earlier and is more pronounced as T_{bot} is increased. As long as the temperatures in the liquid-saturated zone do not exceed the bubble temperature, as discussed in Section 2.4, the flow remains in this second flow regime and exhibits the basic phenomena of the single-phase saturated liquid models reviewed in Section 1.1.

For higher values of T_{bot} the flow starts in the unstable conductive regime and soon starts evolving into the single-phase convection regime. However, before the convection cells are fully developed, the temperature in the hotter portions of the flow exceeds the local bubble temperature and a two-phase zone is initiated. In this zone the temperature holds at the bubble temperature, limiting the development of the convection cell. These two-phase zones expand and settle into a steady state, coexisting with the liquid phase convection cells and forming partial heat pipes. They are characteristic of the third flow regime, which is not exhibited by the simpler single-phase models.

If the heat flux ($J\,m^{-2}\,day^{-1}$) is integrated in the x-direction across the bottom of the (two-dimensional) box, we obtain a global heat transfer rate $Q_{bot}(t)$ ($J\,m^{-1}\,day^{-1}$) that characterizes the rate of uptake of heat at time t by the bed from its isothermal base, per metre in the y-direction (the horizontal direction in which the properties are all assumed uniform.) Similarly, integrating the heat flux across the top of the box, we obtain the heat transfer rate $Q_{top}(t)$ that characterizes the rate of delivery of heat at time t by the bed to its isothermal top.

If the dynamic state of the box approaches a steady state as $t \to \infty$, then both $Q_{bot}(t)$ and $Q_{top}(t)$ approach the steady state heat transfer rate $\bar{Q}(T_{bot})$, which we designate as depending on the parameter of our study, T_{bot}. Four histories of $Q_{bot}(t)$ and $Q_{top}(t)$ are shown in Figure 4 for $T_{bot} = 80$, 100, 120 and 140 °C. For each value of T_{bot}, $Q_{bot}(t)$ is the upper solid curve and $Q_{top}(t)$ is the lower dashed curve. As t approaches 200 years, the upper and lower curves approach each other at a limiting value which defines $\bar{Q}(T_{bot})$ for each case. In Figure 17 of Section 4 a graph of $\bar{Q}(T_{bot})$ versus T_{bot} is given.

There is, of course, a basic difficulty in identifying whether or not a numerical computation of dynamic behaviour has converged to a steady state. In this study we have used inspection of these profiles to make this identification.

In the studies reviewed in Section 1.1 of convection in a saturated zone, the Rayleigh number is used as a basic parameter of study that summarizes the relative importance of buoyancy forces to viscous forces in the fluid. When two phases of the fluid are present in the model, the Rayleigh number is less useful in characterizing the fluid, since the buoyancies and viscosities of the liquid and vapour phases of the liquid are significantly different and the transport is strongly affected by the phase change between them. Moreover, the Rayleigh number does not characterize the fluid, specifically the fraction of the fluid that is in the vapour phase, since the Rayleigh number depends on the temperature difference across the layer but the vapour fraction depends on the absolute temperature and the pressure locally. A less fundamental difficulty with using the Rayleigh number to characterize the saturated zone alone, in the liquid convection regime of our study, is that the upper boundary of the liquid-saturated zone does not have a constant temperature, unlike the studies of saturated zone convection in Section 1.1.

For these reasons we have not tried to use the Rayleigh number as a basic parameter of the study but have selected the bottom temperature for this purpose. To facilitate comparisons, however, a further discussion of the Rayleigh number and the numerical values of the combined physical and geometric data that bear on it for our study is provided in Appendix II.

3.1. Formation of convection cells

For the three higher values of T_{bot} the profiles of $Q_{bot}(t)$ in Figure 4 each show a pulse that is earlier and steeper with increasing T_{bot}. If we examine the temperature distributions during these episodes, we can see that the pulses are associated with the formation of convection cells. Figures 5–8 show the temperature distributions for $T_{bot} = 120$ °C for times 30, 42, 57 and 200 years respectively. Figure 5 shows the temperature essentially independent of x and that the heat is

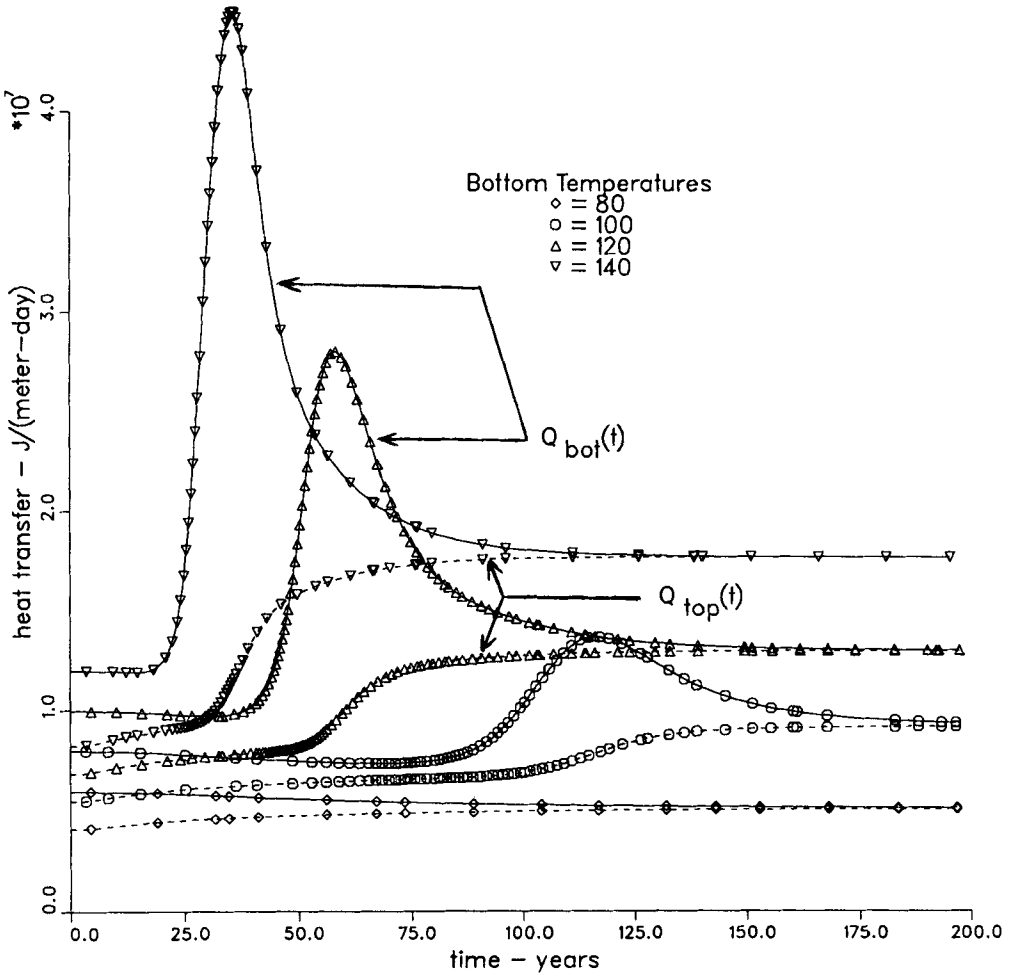

Figure 4. Heat transfer histories

being transferred essentially by conduction. However, the initiation of two 'peaks' and two 'valleys' in the lower portion of the bed is apparent in the temperature distribution at 42 years in Figure 6, and these are highly developed by 57 years, as shown in Figure 7. These peaks of the temperature profile correspond to regions where the hot liquid water is rising from the bottom of the box, and the valleys correspond to regions where the water cooled near the interface with the unsaturated zone is sinking. The peaks and valleys of the temperature profiles internal to the flow field each mark the vertical boundary between two adjacent convection cells of opposite circulation pattern. Since the vertical walls of the box are impermeable, the boundaries at $x=0$ and $x=90$ m each form the boundary of a convection cell. In Figure 7 (and also Figure 8) it can be seen that three cells are present; the boundary at $x=0$ is a region of upwelling of heated water, and the boundary at $x=90$ m is a region of sinking of water cooled in the upper region near the surface of the saturated zone. This can be contrasted with the temperature profile of Figure 13(a) for $T_{bot}=150\,^{\circ}C$. Although the profile is clearly influenced by the vapour phase, two interior

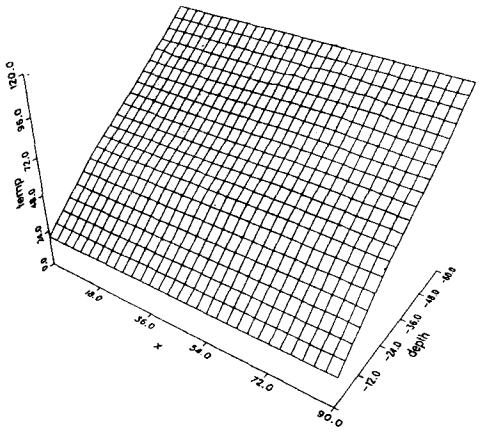

Figure 5. Temperature at 30 years, bottom temperature 120 °C

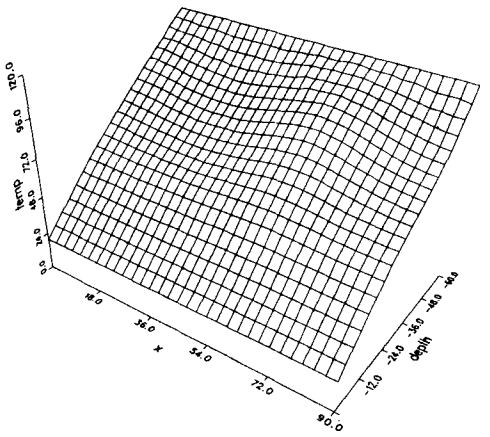

Figure 6. Temperature at 42 years, bottom temperature 120 °C

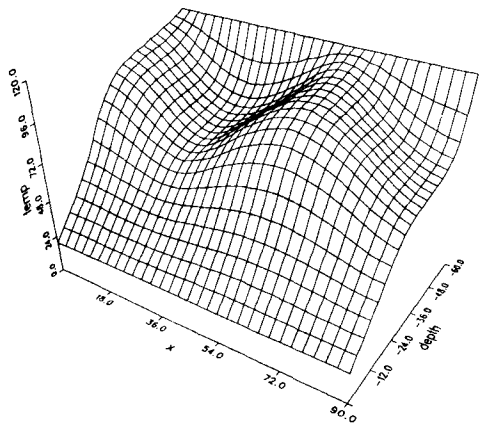

Figure 7. Temperature at 57 years, bottom temperature 120 °C

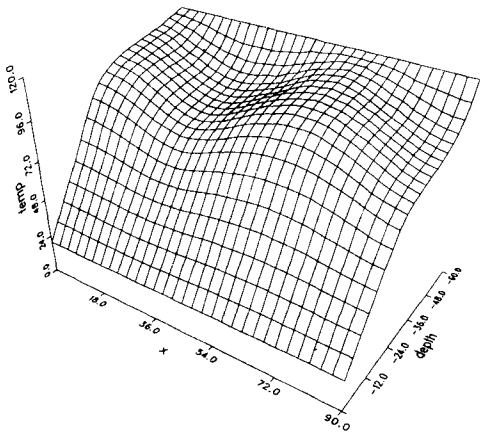

Figure 8. Temperature at 200 years, bottom temperature 120 °C

peaks are clearly present, indicating four convection cells, with cooler water sinking at both boundaries of the box.

Figure 8 shows the steady state temperature profile. Comparison with Figure 7 (the 57 year profile) shows that the temperature valleys of the steady state are higher, as are the peaks, i.e. the temperatures in the convection cells are higher. This difference reflects the convection cell formation mechanisms which explain the pulse in $Q_{bot}(t)$ and the subsequent rise in $Q_{top}(t)$ that appear in Figure 4. The comparison of these temperature profiles can be made in more detail by inspecting the contour plot of Figure 9. In this plot the dashed contours show the temperatures at 57 years and the solid contours show the temperatures at 200 years. The temperatures at 57 years, which is approximately the peak of the pulse, are lower than the steady state temperatures in the cooler regions of sinking liquid, resulting in stronger temperature gradients at the bottom of the layer (e.g. compare the 90 °C contour in both cases.) This results in larger heat transfer rates

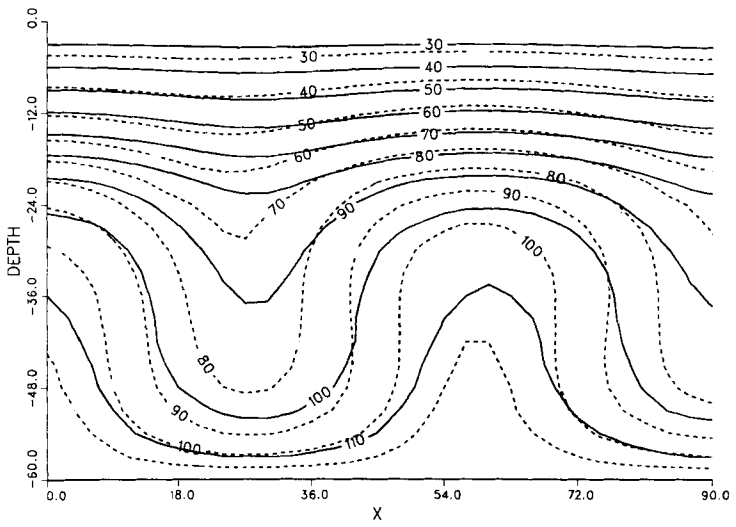

Figure 9. Temperature contours, bottom temperature 120 °C: – – –, at 57 years; ——, at 200 years

through and near the bottom of the layer, resulting in large $Q_{top}(t)$. At this stage the convection has not yet warmed the upper section of the saturated zone and the dashed contours are lower than their solid counterparts of the steady state profile. Hence $Q_{top}(t)$ remains relatively low. The convection subsequently warms the upper parts of the saturated zone, pushing a major portion of the temperature gradient into the overlying unsaturated zone. In these latter stages the water is less cooled in the upper regions of the saturated zone and sinks less vigorously. The temperature contours in the lower part of the layer gradually space apart, reducing $Q_{bot}(t)$, but crowd closer together in the unsaturated zone at the top of the layer, raising $Q_{top}(t)$ until equilibrium is attained. These mechanisms are reflected in the decreasing and increasing segments of the profiles of $Q_{bot}(t)$ and $Q_{top}(t)$ respectively for $t>60$ years in Figure 4.

3.2. The conduction regime

Unlike the three profiles for $Q_{bot}(t)$ and $Q_{top}(t)$ for $T_{bot}=100$, 200 and 140 °C, the profiles of these heat transfer rates for $T_{bot}=80$ °C in Figure 4 show no pulse for $0\leqslant t\leqslant 200$ years but monotonically drop and rise respectively to their limiting value. There is of course no guarantee that a pulse marking the formation of convection cells does not occur for $t>200$ years. Indeed, the temperature distribution for $T_{bot}=80$ °C at constant depth shows a small but regular variation with x, with a maximum total variation of 0·5 °C on the line of depth 40 m. Hence it seems likely that weak convection cells are present or forming. Nevertheless, this effect is so small that it seems appropriate to classify this flow as being in the conduction regime for heat transfer purposes. The same is true for $T_{bot}=85$ °C; however, for $T_{bot}=90$ °C a weak but clearly defined pulse appears in the profile of $Q_{bot}(t)$, which starts its rise at $t=110$ years and peaks at 180 years. The corresponding temperature distribution shows a single internal peak temperature, i.e. a pair of convection cells are formed.

Integration of the dynamic equations is an inefficient way to determine the bifurcation characteristics of the steady state, and it is not clear from these calculations whether there is a critical value of $T_{bot}(\text{crit})$ such that purely conduction solutions exist for the steady state version of this model when $T_{bot}<T_{bot}(\text{crit})$ but convection cells exist for $T_{bot}>T_{bot}(\text{crit})$. Bifurcation and

path continuation techniques[27,28] are designed for this purpose. We can, however, compute Rayleigh numbers for the single-phase (liquid-saturated) layer for $T_{bot}=80$ and 85 °C, which are bottom temperatures close to that at which convection cells become computationally significant, since the temperature is essentially constant at the surface of the saturated zone. These Rayleigh numbers can then be compared with the critical Rayleigh numbers of the single-phase models reviewed in Section 1.1. The single-phase layer is 37 m wide and has upper temperatures of 44·1 and 48·0 °C for $T_{bot}=80$ and 85 °C respectively. On the basis of the definition of Rayleigh number given in Appendix II, the corresponding Rayleigh numbers are 18 and 18·5 respectively. If the critical Rayleigh number is viewed as an approximate indicator of when convection effects start to become significant, then these values can be viewed as being reasonably consistent with the values obtained by Nield,[5] discussed in Section 1.1, which lie in the range 9–27 for the simpler single-phase model and various boundary conditions which could be applied to this layer.

3.3. *Appearance of the vapour phase*

The vapour phase appears in the flow locally where the temperature exceeds the liquid bubble temperature T_{bub} (i.e. the 'boiling' point), which has been discussed in Section 2.5 and is repeated here:

$$T_{bub}(P)=-30{\cdot}0+(P\times 10^{8}/0{\cdot}877)^{1/4{\cdot}76} \quad (°C). \tag{22}$$

The primary variation in pressure is the hydrostatic variation with depth. Hence T_{bub} is significantly depth-dependent. In our modelling the liquid saturation zone starts at a depth of 23 m. The pressure in the overlying unsaturated zone, which we denote by P_0, is slightly variable due to the sealed box conditions, varying from 101 to 105 kPa. Consequently, the hydrostatic pressure in kPa is

$$P_H(z)=\rho_l g(-z-23)+P_0 \quad \text{for} \quad z<-23. \tag{23}$$

For $P_0=100$ the variation of bubble temperature with depth due to the hydrostatic pressure profile of (23) is given in Table I.

Figures 10–12 show several stages in the development of convection cells and two-phase zones for $T_{bot}=150$ °C; part (a) of each figure shows the temperature distribution and part (b) shows the liquid saturation S_l. In Figure 10 the early emergence of convection cells can be seen. In this case four cells are forming, showing two internal upwelling zones or temperature peaks that mark the common boundary of adjacent cells of opposing rotation. In this dynamically unstable evolution the peaks are not identical, however, with the one in the foreground, at $x=65$ m, being hotter. The temperatures in the latter peak reach the local bubble temperature at depths of between 30 and 40 m and a two-phase zone forms within the saturated liquid zone as can be seen in Figure 10(b).

In Figure 11, for $t=28{\cdot}8$ years, the cells are more fully developed. The liquid saturation profile in Figure 11(b) shows that the two-phase zone which was initiated in Figure 10 has expanded and

Table I. Variation of hydrostatic pressure and T_{bub} with depth

z (m)	P_H (kPa)	$T_{bub}(P_H)$ (°C)
30	197	119
40	293	133
50	390	143
60	486	151

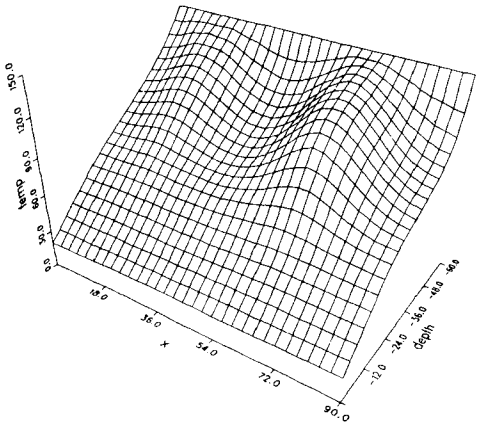

Figure 10(a). Temperature at 24·2 years, bottom temperature 150 °C

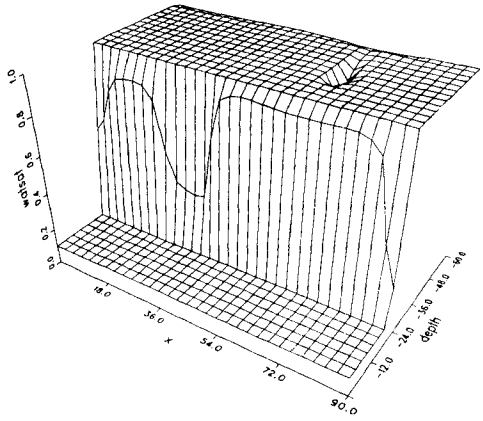

Figure 10(b). Water saturation at 24·2 years, bottom temperature 150 °C

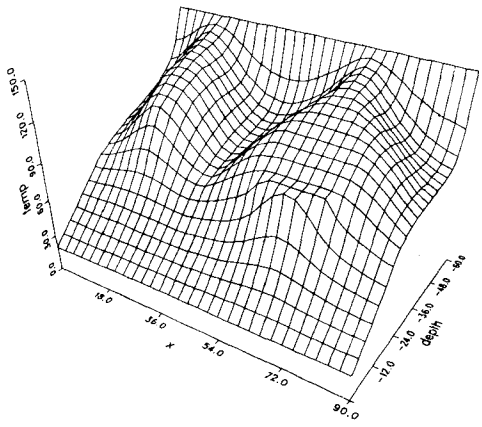

Figure 11(a). Temperature at 28·8 years, bottom temperature 150 °C

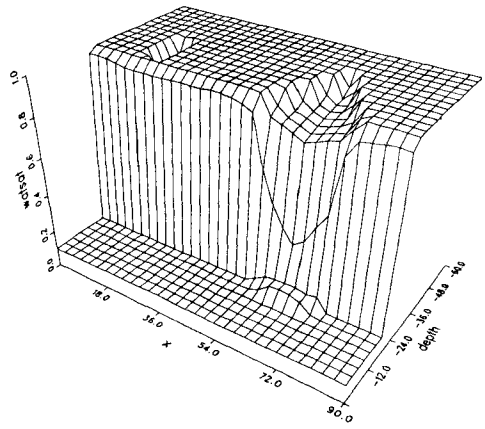

Figure 11(b). Water saturation at 28·8 years, bottom temperature 150 °C

reached the surface of the saturated liquid zone, and the temperatures in the upwelling region centred on $x = 15$ m have reached the local bubble temperatures so that a second internal two-phase zone has appeared. The larger two-phase zone in Figure 11(b) which has burst through the surface of the liquid-saturated region shows a small region of condensation at its top in the overlying unsaturated region. This zone is in the process of forming a heat pipe, evaporating the liquid in its lower, warmer portion and condensing it at the cooler, higher portion. The temperature distribution in this two-phase zone is being constrained by the bubble temperature. In its lower portion the temperature peak is noticeably flattened, since the heat is being used to evaporate the liquid. In the upper portion a small, flat ledge of higher temperatures can be seen in the condensing zone, where the latent heat of condensation is being released. This can also be seen in the contour plot of Figure 12, which shows the temperature distribution at $t = 28{\cdot}8$ years with solid contours and the local bubble temperature with dashed lines. In the upwelling zone at

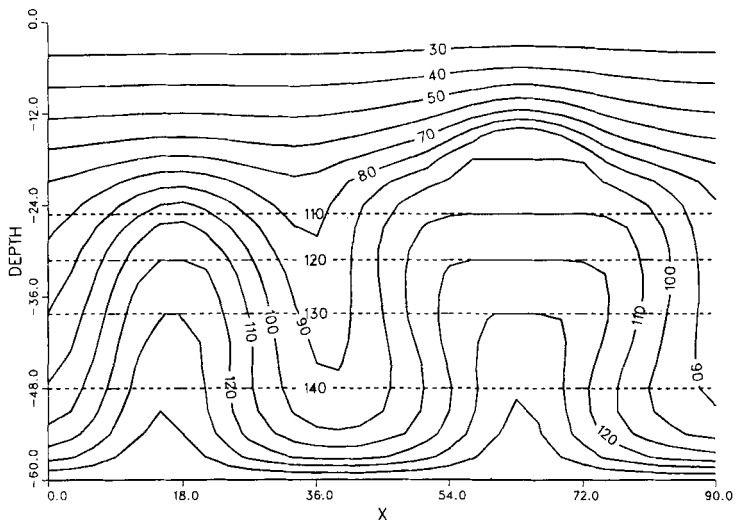

Figure 12. Temperature contours at 28·8 years, bottom temperature 150 °C: – – –, bubble temperature; ——, actual temperature

$x = 65$ m the constraining of the temperature to the local bubble temperature in the two-phase zone is very clear. In the other upwelling zone at $x = 15$ m it can be seen that the temperature contours for $T = 120$ and 130 °C coincide with the local bubble temperature contours of the same values at depths of about 30–40 m, indicating the formation of the second two-phase zone apparent in Figure 11(b). However, in the rest of that region the temperature lies below the local bubble temperatures.

The distributions at 200 years shown in Figure 13 are considered to be the steady state distributions; the two upwelling regions are more closely equal. In each of them a two-phase convection zone has formed which evaporates the liquid in its lower portion in the liquid-saturated zone condenses the vapour in its upper portion in the unsaturated zone. The constraining of the temperature by T_{bub} in both of these zones is clear in Figure 13(a) and in the contour plot of Figure 14, which shows the steady state temperatures as solid contours and the local bubble temperatures as dashed lines.

The asymmetries of Figures 11 and 12 seem to be primarily due to the different rates at which the corresponding pairs of convection cells develop dynamically under these particular initial conditions, perturbations due to terminations of Newton's method, and round-off errors. Figures 13 and 14 also show minor asymmetries between the left and right pairs of convection cells, but these are not due to transient effects since the dynamic changes have essentially died away before 150 years, as shown in Figure 4. The usual mathematical argument for the symmetry of the equilibrium state does not apply here, since it requires uniqueness of the solution which is not present in the instability phenomena for non-linear equations. It is plausible then that there are two different solutions with four convection cells, of which we have computed one.

4. SOME CONCLUSIONS

The two-phase, two-component model appears to be an interesting, computationally viable extension of the single-phase models for heat and fluid transport in a bottom-heated layer of water in a porous medium. It reproduces the phenomena of the simpler model in the appropriate

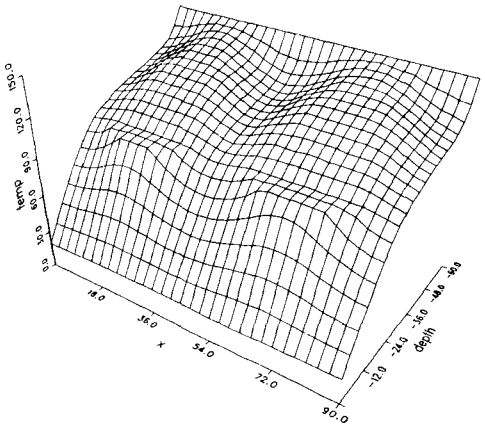

Figure 13(a). Temperature at 200 years, bottom temperature 150 °C

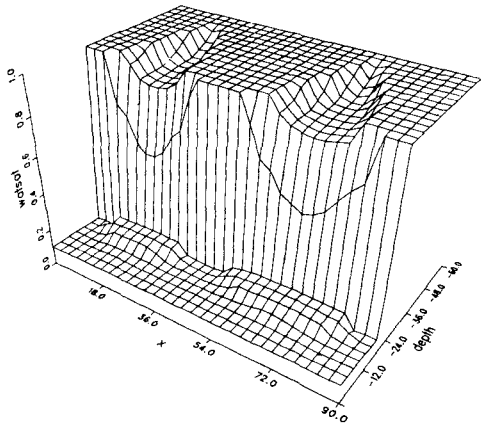

Figure 13(b). Water saturation at 200 years, bottom temperature 150 °C

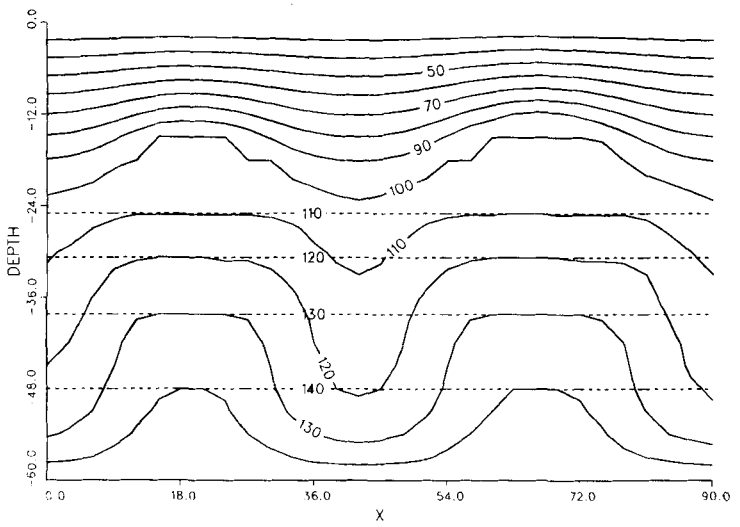

Figure 14. Temperature contours at 200 years, bottom temperature 150 °C: – – –, bubble temperature; ——, actual temperature

heating ranges, and incorporates the phase changes and corresponding alternative heat transport for higher bottom heating. The heat transfer characteristics of the extended model's runs are described in Section 4.2.

We have demonstrated that the two-dimensional extended model on a relatively small mesh, using current numerical techniques, poses a computation that is within the scope of relatively common and inexpensive workstations. The cells of the mesh for solving the extended model's equations were 3 m square; the mesh was 20 cells deep by 30 cells wide. Although several variations in cell size and mesh configuration were checked, no appreciable variation in phenomena was observed and the discretization errors are estimated to be about 5% or less. The running times for the simulations depended heavily on the flow regime. Using a SUN 3/160 with a

WEITEK floating point accelerator (running at about 0·2 Mflops), simulations for the conduction regime took typically 1 h, while simulations for the two-phase convective zone took up to 20 h. Significant further efficiencies could probably be realized by improvements in time step control, particularly in two-phase flows. Because of the complexity of the automatic step size control algorithm for this model, particularly in the presence of changes of state, we interactively modified the time step size control parameters as described in the next subsection.

4.1. Time step size selection

Since each time step involves substantial computations, the appropriate choice of time step size is an important efficiency consideration. This choice is complicated, however, by the dependence of the appropriate time step size on the model's behaviour, i.e. on the current heat transfer regime. In Figure 15 a profile of step size variation for subsequent time steps is shown for $T_{bot} = 150\,^{\circ}C$ for the step size strategy of Section 2.5. In the initial portion of the profile, while the solution is primarily in the conductive regime, the step size grows rapidly if the target change parameters are large enough. As the convection cells start to form and the flow enters the single-phase convection regime, the appropriate step size drops to allow the numerical solution to follow the developing flow. At this stage the most relevant target change parameter is associated with the temperature. If the target change parameters are too high, i.e. are at values appropriate for the conductive

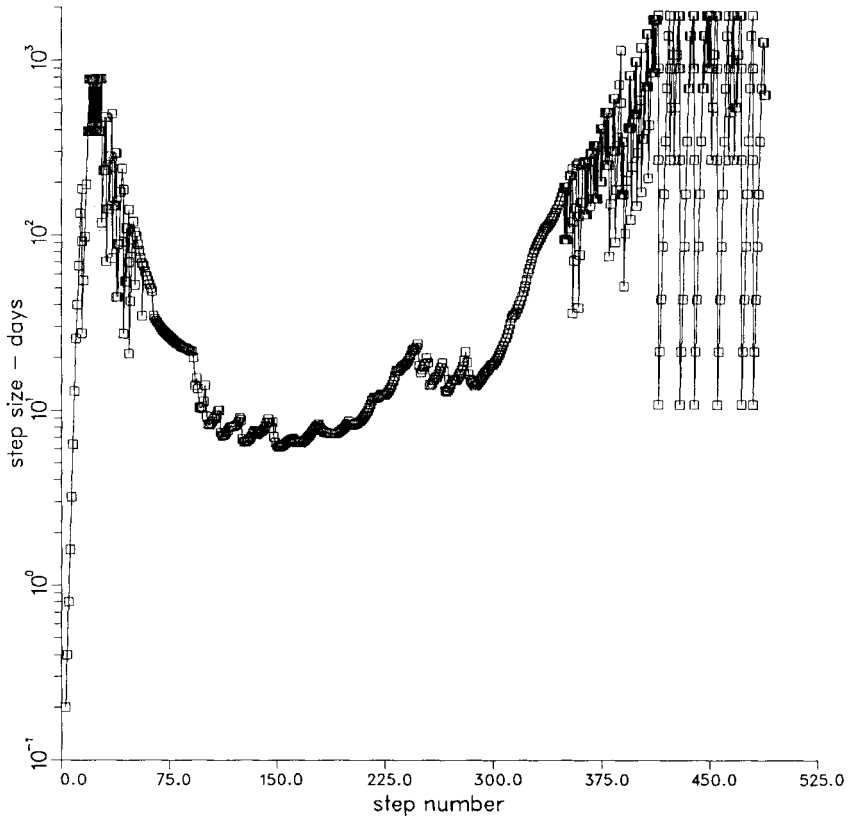

Figure 15. Typical time step size profile for a two-phase problem

regime, then an oscillation in the selected step size will occur, since the projected step size will invariably be too large for the convergence of Newton's iteration. Such oscillations are quite inefficient, since the non-convergent computation with the larger step size is discarded.

If the flow now enters the two-phase convection regime as a result of vaporizing in local 'hot spots' in the liquid convection cells, the appropriate step sizes are typically further reduced due to the degradation of Newton's iteration resulting from primary variable switching. The parameters associated with the saturation variable become more relevant and a further oscillation in selected step size is likely unless the target change parameters are further reduced. As the steady state is approached in the two-phase convection regime, an oscillation in step size is almost unavoidable under this strategy. Small target change parameters admit large step sizes as the steady state is approached; however, a number of mesh cells are close to the bubble temperature, and for these cells, primary variable switching can occur at each Newton iteration, preventing convergence unless the step size is small enough.

Rather than attempt to develop adaptive algorithms for controlling the time step size selection parameters, we elected to implement a technique for monitoring the calculation and modifying these parameters appropriately for the current state of the solution. The technique involves two files for the executing programme: the monitoring file and the current parameters file. The executing programme writes details of each Newton iteration in the monitoring file, which we can review to check the progress of the computation using the current parameter values. If we wish to change the current parameters, we first lock the executing programme out from reading the current parameters file, change the parameter values with a text editor and then unlock the access by the executing programme. On the executing programme side, immediately prior to computing a provisional time step as described above, the programme determines whether it is locked out

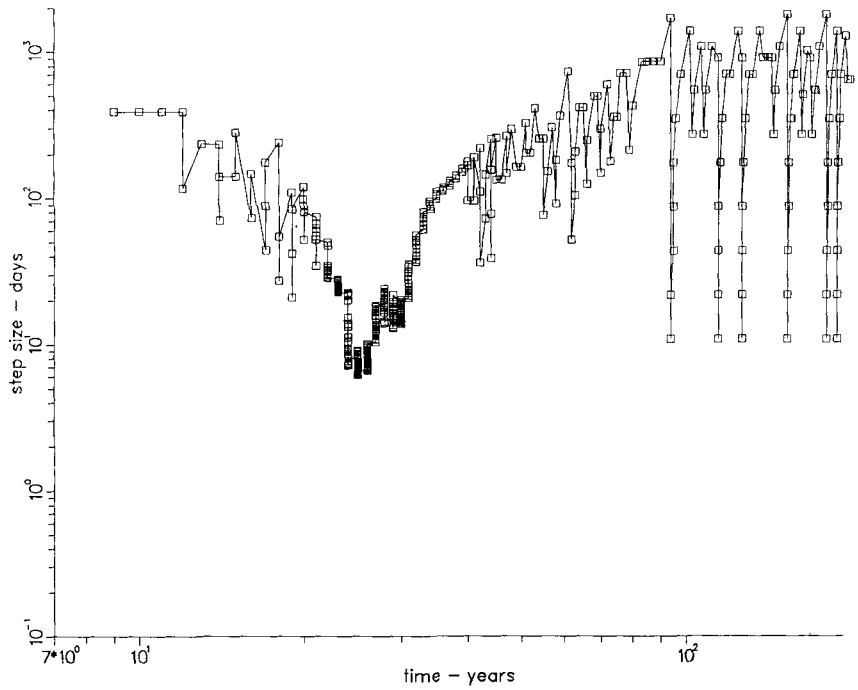

Figure 16. Time step size profile as a function of absolute time

from reading the current parameters file. If it is not, then it reads their values in (which may or may not have been modified) and uses them to compute the provisional time step; if it is locked out, it uses the existing internal parameter values.

This technique allows the executing programme to run for long periods of time unattended but for a user to modify the parameters at will. A third file, called a lockfile, can be used to provide the locking/unlocking mechanism in a manner that conforms to the FORTRAN 77 standard. To lock the programme we create the lockfile (which may be empty) and to unlock it we delete the lockfile. The programme issues an INQUIRE command to determine if the lockfile is present in the file directory. If it is present, then the programme knows it is locked out of the current parameters file.

The time step profiles shown in Figures 15 and 16 were obtained for $T_{bot} = 150\,^{\circ}C$ using this monitoring parameter-modifying technique. The sudden drops in the step size at about steps 50 and 100 are due to decreases in the temperature target change parameter at those stages. The inefficient oscillation in the time step size at the end of the run is clearly in evidence. The programme was simply left to run at that stage.

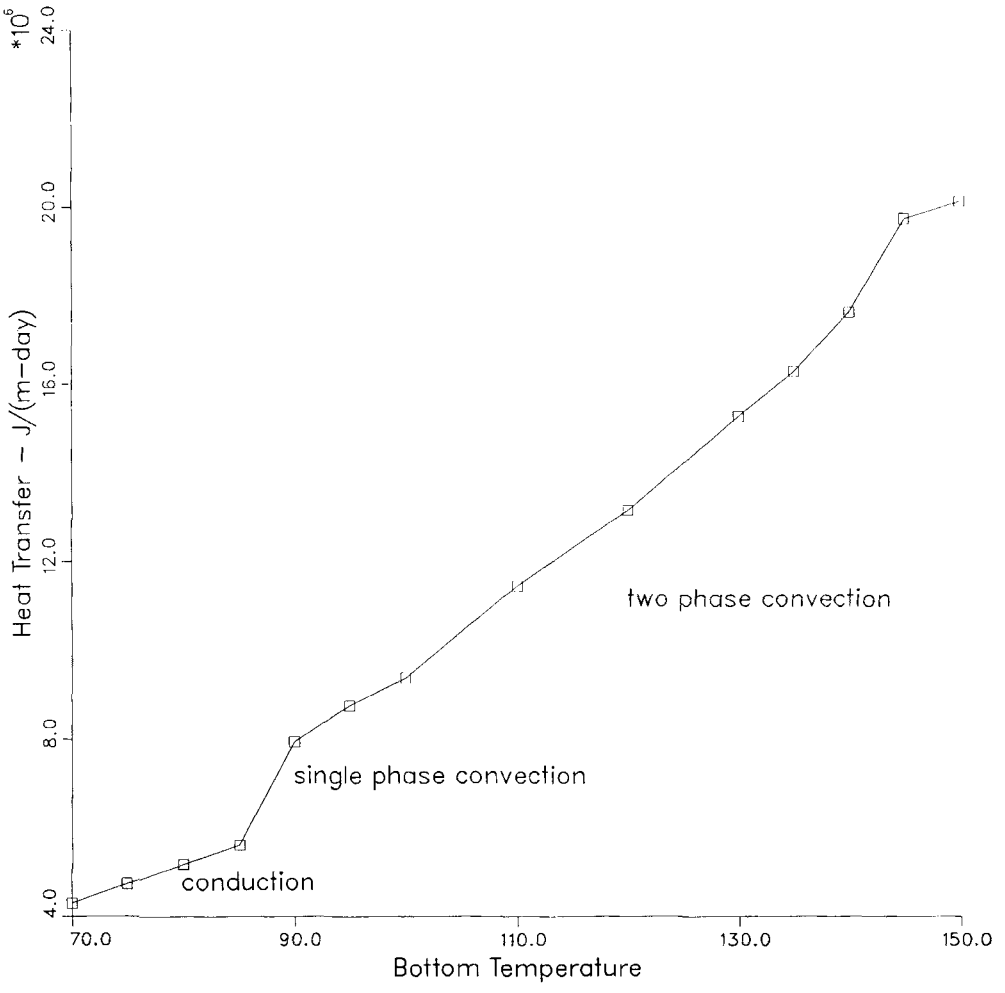

Figure 17. Heat transfer characteristics

4.2. Heat transfer characteristics

Using the basic, dimensioned parameters of this study, we can observe the heat transfer characteristics for this model in Figure 17, where the bottom temperature is plotted against the steady state heat transfer rate $\bar{Q}(T_{bot})$ as defined in Section 3. In this plot, four values of T_{bot} have been used in each of the conduction regimes (70–85 °C) and five values in each of the single-phase convection regimes (90–120 °C) and the two-phase convection regime (130–150 °C).

The well-known role of convection in enhancing heat transfer in the single-phase convection regime, as reviewed in Section 1.1 and the referenced literature, is evident in Figure 17.

In the two-phase convection regime, two new effects are encountered which work counter to each other. Firstly, the phase change inhibits the effectiveness of the convection cells for heat transfer in the liquid phase by capping the temperature at T_{bub} and disrupting the flow pattern of the cell. On the other hand, the partial heat pipe that forms in the two-phase zones enhances the heat transfer. It is not clear from Figure 17 which of these effects dominates; the heat transfer rate rises fairly sharply up to 145 °C and then appears to level off somewhat, which coincides with a change in steady state solution structure from three convection cells to four.

At higher bottom heating a vapour layer forms at the lower boundary. While this is a very interesting phenomenon, we feel that the isothermal bottom model is inappropriate for its study, because the solution behaviour becomes very temperature-sensitive as T_{bot} approaches T_{bub}. It seems to us that a constant-heat-flux lower boundary condition would be more suited to the study of vapour formation at the bottom of a heated bed.

ACKNOWLEDGEMENTS

This work was supported by the government of Ontario through the Information Technology Research Centre and by the Natural Science and Engineering Research Council of Canada.

APPENDIX I

This appendix gives values of the parameters and the correlations used for various physical properties of the extended model. As in Section 2, the following subscript associations are followed: w, water; a, air; R, rock; l, liquid phase; g, gas phase; s, reference standard.

Pressure

$$P \quad \text{(kPa)}.$$

Molar densities

$$M_w = M_{ws}[1 + \alpha_w(P - P_s) - \beta_w(T - T_s)] \quad \text{(mole m}^{-3}\text{)},$$

$$M_{ws} = 5{\cdot}55 \times 10^4 \text{ mole m}^{-3}, \qquad \alpha_w = 4{\cdot}3 \times 10^{-6} \text{ kPa}^{-1}, \qquad \beta_w = 2{\cdot}5 \times 10^{-4} \text{ K}^{-1},$$

$$T_s = 273 \text{ K}, \qquad P_s = 100 \text{ kPa}, \qquad M_g = P/RT \quad \text{(mole m}^{-3}\text{)},$$

$$R = 8{\cdot}314 \times 10^{-3} \text{ kPa m}^3 \text{ mole}^{-1} \text{ K}^{-1}.$$

Mass density

$$\rho_l = M_w(W_w X_w + W_a X_a) \quad \text{(kg m}^{-3}\text{)}, \qquad \rho_g = M_g(W_w Y_w + W_a Y_a) \quad \text{(kg m}^{-3}\text{)},$$

$$W_w = 18{\cdot}02 \times 10^{-3} \text{ kg mole}^{-1}, \qquad W_a = 28{\cdot}97 \times 10^{-3} \text{ kg mole}^{-1}.$$

Equilibrium ratios

$$Y_a = Z_a X_a, \qquad Y_w = Z_w X_w, \qquad Z_a = 1 \times 10^9/(7{\cdot}6P\alpha^*),$$

where α^* is linearly interpolated from Table II,

$$Z_w = [0{\cdot}8777 \times 10^{-8}(T-243)^{4{\cdot}76}]/P.$$

Enthalpies

$$h_l = C_w(T-T_s)X_w + C_a(T-T_s)X_a \quad (\text{J mole}^{-1}),$$

$$C_w = 75{\cdot}4 \text{ J mole}^{-1}\text{ K}^{-1}, \qquad C_a = 29{\cdot}2 \text{ J mole}^{-1}\text{ K}^{-1}, \qquad T_s = 273 \text{ K},$$

$$h_{ga} = C_a(T-T_s) \quad (\text{J mole}^{-1}), \qquad H_{gw} = C_w(T-T_s) + h_{lat} \quad (\text{J mole}^{-1}),$$

$$h_{lat} = \begin{cases} 4{\cdot}814 \times 10^3(T_c - T)^{0{\cdot}38}, & T < T_c \quad (\text{J mole}^{-1}), \\ 0, & T > T_c, \end{cases}$$

$$T_c = 647{\cdot}3 \text{ K}, \qquad h_g = Y_w h_{hw} + Y_a h_{ga}.$$

Internal energies

$$U_w = h_w - (P \times 10^3)/M_w \quad (\text{J mole}^{-1}), \qquad U_g = h_g - (P \times 10^3)/M_g \quad (\text{J mole}^{-1}).$$

Heat capacity of rock

$$U_R M_R = 2{\cdot}35 \times 10^6 \text{ J m}^{-3}\text{ K}^{-1}.$$

Viscosities

$$\mu_l = 10^{-9}/[12{\cdot}1 + 2{\cdot}88(T-T_s) + 7{\cdot}78 \times 10^{-4}(T-T_s)^2] \quad (\text{kPa day}),$$

$$\mu_g = 10^{-13}[1{\cdot}574 + 0{\cdot}0044(T-T_s)] \quad (\text{kPa day}).$$

Gas phase diffusivity[19]

$$D_g = D_g^0 \phi S_g (T/273)^{2{\cdot}334}/(P/100).$$

Permeabilities

Absolute permeability $K = 10^{-12}$ m^2. The relative permeabilities in the unsaturated states are obtained by linear interpolation in Table III.

Porosity

$$\phi = 0{\cdot}4.$$

Table II. Parameter α^* for computing Z_a

T (K)	α^*
273	30·5
293	19·8
323	13·9

Table III. Unsaturated zone relative permeabilities

S_l	K_{rw}	K_{rg}
0·0	0·0	1·6
0·15	0·0	1·0
0·2	0·0002	0·83
0·4	0·02	0·35
0·6	0·148	0·104
0·8	0·447	0·013
0·9	0·68	0·001
0·95	0·83	0·0002
1·0	1·0	0·0

Effective heat conductivity

$$\lambda_H=(1-\phi)\lambda_r+\phi S_l\lambda_w, \quad \lambda_r=7{\cdot}0\times10^4\ \mathrm{J\ m^{-3}\ K^{-1}\ day^{-1}}, \quad \lambda_w=5{\cdot}35\times10^4\ \mathrm{J\ m^{-3}\ K^{-1}\ day^{-1}}.$$

Gravitational acceleration

$$g=9{\cdot}8066\ \mathrm{m\ s^{-2}}.$$

APPENDIX II

In the introduction to Section 3, an explanation is presented for why we feel the Rayleigh number is an inappropriate basic parameter for this study involving a fluid that is an evaporating two-phase liquid. However, to help facilitate comparisons with other work, particularly for the liquid phase convection regime, we present the following derivation. The Rayleigh number for a horizontal liquid-saturated layer ($S_l=1$) is defined to be

$$Ra=b\beta_w C_w g M_{ws} K(T_{bot}-T_{top})/\nu\lambda_H.$$

In addition to the symbols given in Appendix I, this formula requires b (liquid-saturated layer thickness) = 37 m, ν (kinematic viscosity of water) = $10^{-6}\ \mathrm{m^2\ s^{-1}}$ and $\lambda_H=0{\cdot}7624\ \mathrm{J\ K^{-1}\ m^{-1}\ s^{-1}}$ (repeated for $S_l=1$ in units required for Ra). Evaluation of Ra for the parameter values given here and in Appendix I results in

$$Ra=0{\cdot}5(T_{bot}-T_{top}).$$

REFERENCES

1. H. C. Hardee and R. H. Nilson, 'Natural convection in porous media with heat generation', *Nucl. Sci. Eng.*, **63**, 119–132 (1977).
2. J. P. Caltagirone, 'Thermoconvective instabilities in a horizontal porous layer', *J Fluid Mech.*, **72**, 269–287 (1975).
3. M. A. Combarnous and S. A. Bories, 'Hydrothermal convection in saturated porous media', *Adv. Hydrosci.*, **10**, 231–307 (1975).
4. P. Cheng, 'Heat transfer in geothermal systems', *Adv. Heat Transfer*, **14**, 1–105 (1978).
5. D. A. Nield, 'Onset of thermohaline convection in a porous medium', *Water Resources Res.*, **4**, 553–560 (1968).
6. S. L. Moya, E. Ramos and M. Sen, 'Numerical study of natural convection in a tilted rectangular porous material', *Int. J. Heat Mass Transfer*, **30**, 741–756 (1987).
7. M. Sen, P. Vasseur and L. Robillard, 'Multiple steady states for unicellular natural convection in an inclined porous layer', *Int. J. Heat Mass Transfer*, **30**, 2097–2113 (1987).
8. J. P. Caltagirone and S. Bories, 'Solutions and stability criteria of natural convective flow in an inclined porous layer', *J. Fluid Mech.*, **155**, 267–287 (1985).

9. B. Borkowska-Pawlak and W. Kordylewski, 'Stability of two-dimensional natural convection in a porous layer', *Mech. Appl. Math.*, **35**, 279–290 (1982).
10. S. Kimura, G. Schubert and J. M. Straus, 'Route to chaos in porous-medium thermal convection', *J. Fluid Mech.*, **166**, 305–324 (1986).
11. Y. F. Rao, K. Fukuda and S. Hasegawa, 'A numerical study of three-dimensional natural convection in a horizontal porous annulus with Galerkin method', *Int. J. Heat Mass Transfer*, **31**, 695–707 (1988).
12. M. R. Davidson, 'Natural convection of gas/vapour mixtures in a porous medium', *Int. J. Heat Mass Transfer*, **29**, 1371–1381 (1986).
13. C. H. Lai, G. S. Bodvarsson and P. A. Witherspoon, 'Second-order upwind differencing method for nonisothermal chemical transport in porous media', *Numer. Heat Transfer*, **9**, 453–472 (1986).
14. C. H. Sondergeld and D. L. Turcotte, 'An experimental study of two-phase convection in a porous medium with applications to geological problems', *J. Geophys. Res.*, **82**, 2045–2053 (1977).
15. G. Schubert and J. M. Straus, 'Gravitational stability of water over steam in vapor-dominated geothermal systems', *J. Geophys. Res.*, **85**, 6505–6512 (1980).
16. H. H. Bau and K. E. Torrance, 'Boiling in low-permeability porous materials', *Int. J. Heat Mass Transfer*, **25**, 45–55 (1982).
17. K. S. Udell, 'Heat transfer in porous media considering phase change and capillarity—the heat pipe effect', *Int. J. Heat Mass Transfer*, **28**, 485–495 (1985).
18. D. W. Pollock, 'Simulation of fluid flow and energy transport processes associated with high-level radioactive waste disposal in unsaturated alluvium', *Water Resources Res.*, **22**, 765–775 (1986).
19. Y. W. Tsang and K. Pruess, 'A study of thermally induced convection near a high-level waste repository in partially saturated fractured tuff', *Water Resources Res.*, **23**, 1958–1966 (1987).
20. K. Pruess, 'Modeling of geothermal reservoirs: fundamental processes, computer simulation and field applications', *Geothermics*, **19**, 3–15 (1990).
21. P. A. Forsyth, 'Radioactive waste disposal heating effects in unsaturated fractured rock', *Numer. Heat Transfer*, **17**, 29–51 (1990).
22. G. A. Behie and P. A. Forsyth, 'Incomplete factorization methods for fully implicit simulation of enhanced oil recovery', *SIAM J. Sci. Stat. Comput.*, **5**, 543–561 (1984).
23. J. R. Kightley and P. A. Forsyth, *WATSIT Iterative Sparse Matrix Solver: User's Guide.*, Department of Computer Science, University of Waterloo, 1989.
24. B. Rubin and W. Buchanan, 'A general purpose thermal model', Paper SPE 11713 presented at The California Regional Meeting, 1983, Ventura, California.
25. J. A. Trangenstein and J. B. Bell, 'Mathematical structure of compositional reservoir simulation', *SIAM J. Sci. Stat. Comput.*, **10**, 817–845 (1989).
26. K. Eriksson and C. Johnson, 'Error estimates and automatic time step control for nonlinear parabolic problems, I', *SIAM J. Numer. Anal.*, **24**, 12–23 (1987).
27. R. Glowinski, H. B. Keller and L. Reinhart, 'Continuation-conjugate gradient methods for the least squares solution of nonlinear boundary value problems', *SIAM J. Sci. Stat. Comput.*, **6**, 793–832 (1985).
28. R. Seydel, *From Equilibrium to Chaos—Practical Bifurcation and Stability Analysis*, Elsevier, Amsterdam, 1988.